Measuring Local Optical Properties: Near-Field Polarimetry of Photonic Block Copolymer Morphology

M. J. Fasolka,* Lori S. Goldner,† and J. Hwang

Optical Technology Division, National Institute of Standards and Technology, Gaithersburg, Maryland 20899-8441

A. M. Urbas, P. DeRege, T. Swager, and E. L. Thomas

*Departments of Materials Science and Engineering and Chemistry, Massachusetts Institute of Technology,
Cambridge, Massachusetts 02139*

Ultrahigh molecular weight polystyrene-*b*-polyisoprene block copolymers (BCs), noted for their photonic behavior, were imaged using transmission near-field scanning optical microscopy (NSOM) and NSOM polarimetry. Our improved scheme for polarization modulation (PM) polarimetry, which accounts for optical anisotropies of the NSOM aperture probe, enables mapping of the local diattenuation and birefringence (with separately aligned diattenuating and fast axes) in these specimens with subdiffraction limited resolution. PM-NSOM micrographs illuminate the mesoscopic optical nature of these BC specimens by resolving *individual* microphase domains and defect structures.

Mesoscopic self-assembly is widely recognized as a route to photonic band gap materials, as demonstrated by naturally occurring opals and synthetic systems created through, e.g., the colloidal assembly and/or phase separation of both organic and inorganic molecules and particles [1]. In this regard, block copolymers (BCs) offer a particularly versatile way of creating the patterned arrays of refractive index required for photonic properties [2,3]. BC microphase separation, driven by the immiscibility of the end-connected constituent polymer chains or *blocks*, produces a variety of domain motifs (lamellae, double-gyroid, hexagonal-packed cylinders and bcc spheres) with a related set of one-, two- and three-dimensional band structures [2,4], tunable through the BC composition [5]. A BC's molecular mass (M_r) governs the microphase domain periodicity (L_0), typically limited to a range of 10 to 100 nm. However, recent synthetic efforts have produced ultrahigh molecular mass BCs with L_0 values of 150 to 300 nm, enabling M_r-tailored photonic band gaps in the visible range [3]. This morphological flexibility is complimented by an extensive set of techniques geared to perfect/control the order of BC structures and furnish them with added functionality [6]. These strategies can be harnessed to enhance the optical performance of BC materials and devices based upon them.

Since the optical activity of single microphase domains and defect structures may dictate device function, the advancement of photonic BC systems requires characterization of their optical properties at the mesoscopic level. While traditional spectroscopies and far-field microscopy are adequate for measuring the bulk/ensemble optical qualities of photonic materials, they lack the spatial resolution required to map these properties on the mesoscale. NSOM enables such measurements via its subdiffraction

limit resolution [7,8]. We present here the first optical micrographs of BC morphology, collected using *visible-light* aperture NSOM. In addition, an improved NSOM polarimetry enables local optical properties (birefringence, diattenuation, and the separate alignment angles of the fast and diattenuating axes) to be mapped simultaneously. These measurements, resolved on the length scale of single BC microphase domains/defects, represent a novel means of examining these materials *with the wavelengths relevant to their use.*

Transmission aperture NSOM achieves super resolution by illuminating a thin specimen with light confined to a subwavelength aperture, typically 50 to 150 nm wide [7,8]. By positioning the sample in the near field of the aperture, the confined light transmits the sample to be collected via conventional optics. Micrographs, acquired by scanning the sample and measuring the transmitted intensity at each point, exhibit resolution determined by the aperture width. While scanning the sample to aperture distance is maintained to ≤ 10 nm using a shear-force feedback system [9], which also yields the sample topography.

Our polarimetric measurements are built upon polarization modulation (PM) schemes [10] adapted to NSOM by McDaniel and Hsu [11,12]. A laser source (488 nm) is conditioned by a linear polarizer (LP, at 0°), followed by a photoelastic modulator (PEM, modulation axis −45°) and quarter wave retarder (QWR, fast axis −90°). This produces linearly polarized light whose polarization direction oscillates with frequency, $\omega/2\pi$ (50 kHz), and amplitude, d, controlled by the PEM. This source light is injected into the NSOM probe fiber via a fiber coupler. Stress-induced birefringence in the fiber is controlled with a fiber polarization controller ("fiber paddles"). Fourier decomposition of the transmitted intensity yields

the sample diattenuation, or if a post-sample circular analyzer, A1 (QWR, fast axis $0°$, followed by LP at $-45°$), is in place, the sample birefringence. NSOM fiber probes were fabricated as in [8] with apertures 100 to 125 nm wide. Transmitted light is collected with a 0.85 NA objective and directed to a photomultiplier tube detector. Instrumental details can be found in Refs. [13,14].

Extraction of specimen optical properties via PM-NSOM requires measurement and analysis methods that compensate for optical anisotropies in the aperture and the probe's fiber tail. Practically all NSOM apertures exhibit diattenuation [15,16]. Recently, Wei and Fann outlined schemes to correct for probe diattenuation in sample diattenuation measurements [16], and Campillo *et al.* [17] show how to account for probe and specimen in birefringence measurements *if* the specimen's diattenuating axis and fast axis are aligned. We elucidate all of these effects *without* the assumption of aligned axes. In addition, while stress-induced birefringence in a bare optical fiber can be balanced (i.e.,"nulled") via fiber paddles [11], we show that this nulling results in a residual birefringence when done on fibers equipped with a diattenuating aperture [14]. Our procedures and analysis fully account for these optical anisotropies in the NSOM probe.

A complete description of our approach requires a longer publication [14]; here we supply the final analysis formalism and outline our experimental protocols. Fourier series expansion of the measured intensity (I) yields the following: $I(t) = A_0 + A_1 \sin(\omega t) + A_2 \cos(2\omega t) + \dots$. Given tip and sample retardance ≤ 0.1 rad, and tip and sample diattenuation ≤ 0.1 (i.e., thin specimens and quality probes), we can write (using a Jones or Mueller formalism and including terms with an accuracy of order 1%)

$$R_{1\omega} \equiv \frac{A_1}{A_0} \cong 2J_1(d)[D_t \sin(2\varphi_d^t) + D_s \sin(2\varphi_d^s)], \quad (1)$$

$$R_{2\omega} \equiv \frac{A_2}{A_0} \cong 2J_2(d)[D_t \cos(2\varphi_d^t) + D_s \cos(2\varphi_d^s)], \quad (2)$$

and with A1 in place (a "birefringence" measurement):

$$B_{1\omega} \equiv \frac{A_1}{A_0} \cong R_{1\omega} + 2J_1(d)[\sin(\theta_t)\cos(2\varphi_b^t) + \sin(\theta_s)\cos(2\varphi_b^s)], \quad (3)$$

$$B_{2\omega} \equiv \frac{A_2}{A_0} \cong R_{2\omega} - 2J_2(d)[\sin(\theta_t)\sin(2\varphi_b^t) + \sin(\theta_s)\sin(2\varphi_b^s)], \quad (4)$$

Here $D_t(D_s)$ is the diattenuation of the tip (sample), φ_d^t (φ_d^s) is the relative angle of the tip (sample) diattenuating axis, θ_t (θ_s) is the retardance across the tip (sample), and φ_b^t (φ_b^s) is the angle of the tip's (sample's) fast axis. J_1 and J_2 are first- and second-order Bessel functions, $d = 2.405$ rad is the PM amplitude [chosen for $J_0(d) = 0$],

and A_0 is the dc (transmission) intensity. The diattenuation is $D = (q - r)/(q + r)$, where q and r are the intensity transmission coefficients for light polarized along and perpendicular to the diattenuating axis. In our experiments A_0, A_1, and A_2 are extracted via Fourier analysis of the intensity signal and used to compute the polarimetric quantities using Eqs. (1)–(4).

With no sample in place and A1 inserted, the polarimeter output is nulled using fiber paddles (a discussion of nulling is found in Refs. [11,14]). Then, with A1 removed, D_t and θ_t are determined by measuring $R_{1\omega}$ and $R_{2\omega}$ and using Eqs. (1) and (2) (here, $D_s = \theta_s = 0$). Next, with A1 in, we measure $B_{1\omega}$ and $B_{2\omega}$, subtract $R_{1\omega}$ and $R_{2\omega}$, respectively, and solve for the residual θ_t and φ_b^t. Now, the sample is installed and the two measurements (A1-in and A1-out) are repeated in separate 128 by 128-point scans. Afterwards, the tip properties are remeasured to ensure that they have not changed. The sample properties are calculated using the full set of measurements. Topography or transmission images are used to align the two optical measurements, accounting for positional drift. Because of circular birefringence in the fiber, absolute angular information is lost [11], so φ_d^s and φ_b^s are *relative* angular values.

Figure 1 shows a transmission NSOM micrograph of a photonic polystyrene-*b*-polyisoprene (PS-*b*-PI) block copolymer specimen. Produced via living anionic polymerization in a nitrogen drybox, this material ($M_r = 1.4 \times 10^6$) is nearly volume symmetric in composition (PS/PI = 480 K/560 K), and exhibits the lamellar microdomain motif with $L_0 = 240$ nm. Bulk specimens were processed by roll casting, which helps order and align the microphase domains [18]. Thin (100 nm) sections were sliced from the bulk using cryo-ultramicrotomy and deposited onto glass coverslips. Subsequent exposure to OsO_4 vapor (2 h) preferentially crosslinks the PI domains, making them less mechanically compliant (more amenable to shear-force feedback), and enhancing the optical contrast between PS and PI. In addition, this processing may mirror absorptive effects inherent to doping strategies, e.g., sequestration of nanoparticles or chromophores into BC domains. Single lamellar domains and defects are readily resolved in transmission (Fig. 1, top). The PI domains (lightly stained, $n = 1.52$) appear darker, while PS domains ($n = 1.59$) are lighter, as verified through the topography image and plot (Fig. 1, middle, bottom), which demonstrate that darker domains are also lower in height, due to PI contraction during OsO_4 crosslinking. Interestingly, while well-ordered lamella show modest interdomain optical contrast ($\approx 10\%$), defect structures such as edge dislocations (*a*) and lamellar separations (*b*) exhibit exaggerated contrast. These defects may locally attenuate transmission through scattering, or decrease the amount of light coupled from the aperture. Similar effects are observed in NSOM studies of holes in dielectric films [19]. In our study, this contrast highlights defects and
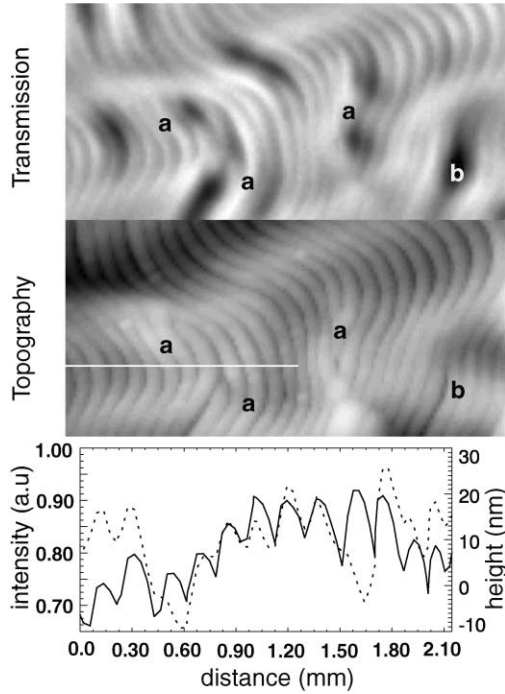
FIG. 1. NSOM images of PS-*b*-PI BC. Transmission (top), topography (middle). The plot (bottom) shows topography (solid) and transmission (dashed) along the white line (2.1 μm) in the topography image, smoothed over a three-pixel bin. Labels *a* and *b* show edge dislocations and lamellar separations, respectively.
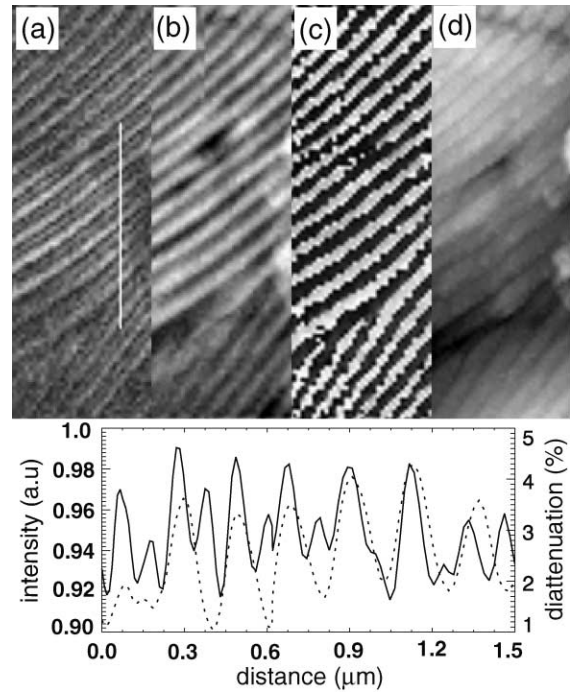

FIG. 2. PM-NSOM images of PS-*b*-PI BC. Color scale ranges given as [minimum, maximum]. (a) Diattenuation [0%, 5%]; (b) transmission (normalized intensity) [0.6, 1.0]; (c) diatten-uation angle [0°, 180°]; topography [0 nm, 25 nm]. The bottom plot shows transmission (dotted) and diattenuation (solid) along white line (1.5 μm) in (a), smoothed over a three-pixel bin.

confirms the notion that they may adversely affect the performance of these materials in photonic devices.

Figure 2 maps the diattenuation of a BC specimen [calculated via Eqs. (1) and (2)] with the simultaneously acquired topography and transmission micrographs. Note that the optical images [Figs. 2(a)–2(c)], in particular, the image of D_s [Fig. 2(a)], provide excellent morpho-logical detail. Comparison of D_s [Fig. 2(a)] and trans-mission [Fig. 2(b)] along the white line (Fig. 2, bottom) show that the higher-transmitting PS domains have larger D_s (3% to 5%), the absorbing PI domains have smaller D_s (2% to 4%), and that D_s is minimized near the domain interface. An explanation for this pattern of D_s is sug-gested by the Bethe-Bowkamp model (BB) [20], which approximates the field emanating from an NSOM aper-ture. In this model, a field polarized along a given axis is elongated along that axis. This anisotropic field, centered over an absorbing PI domain, transmits less/more when polarized parallel/perpendicular to the domain, produc-ing an apparent diattenuation [14]. For the less absorbing PS domains, the opposite is true. Indeed, φ_d^s [Fig. 2(c)] alternates between domains with a difference $\approx 90°$.

The full range of measurements is shown in Fig. 3, which focuses on a symmetric tilt boundary where the lamella bend through two "kinks" along an "N"-shaped track. In these micrographs, the D_s images (*c, e*) are used (with probe data) to correct the birefringence images (*d, f*), via Eqs. (3) and (4). As in Fig. 2, the D_s image

[Fig. 3(c)] illuminates the domain and interface morphol-ogy across the defect. The retardance (θ_s) is mapped in Fig. 3(d). The standard uncertainty is $\pm 0.6°$ [14]. In principle, contrast here is governed by the equation, $\theta_s = ft\Delta n/\lambda$, which relates θ_s to the sample thickness (*t*), the intrinsic birefringence (Δn), the illumination wavelength ($\lambda = 488$ nm), and the degree of chain orientation (*f*) [21]. Interdomain contrast is therefore based upon the difference in Δn between PS ($\Delta n = 0.195$) [21] and PI ($\Delta n = 0.13$) [22], and *f*, which reflects the net average elongation of chains perpendicular to the interface ex-hibited by ordered BC systems. Thus, in compari-son PS domains are lighter (larger θ_s), while PI domains are darker, as verified by comparing Fig. 3(d) with Fig. 3(b). Contrast across the defect is dictated by *f* and *t*. In principle θ_s is proportional to the local stress (through *f*), but variations in the through-plane lamellar orienta-tion, i.e., "projection effects" due to arbitrary sectioning of the specimen, may also affect θ_s. Indeed, as expected with projection effects, θ_s often seems inversely related to the apparent L_0 observed in this image. In-plane lamellar orientation is illuminated in Fig. 3(f), which maps the relative φ_b^s. In BCs, φ_b^s reflects the orientation of the low-*n* axis, which due to chain elongation lies perpen-dicular to the domain interface. As the lamellae bend through the symmetric tilt boundary, φ_b^s increases and decreases accordingly. Discontinuities in the φ_b^s image are due to phase wrapping. While previous polarimetric
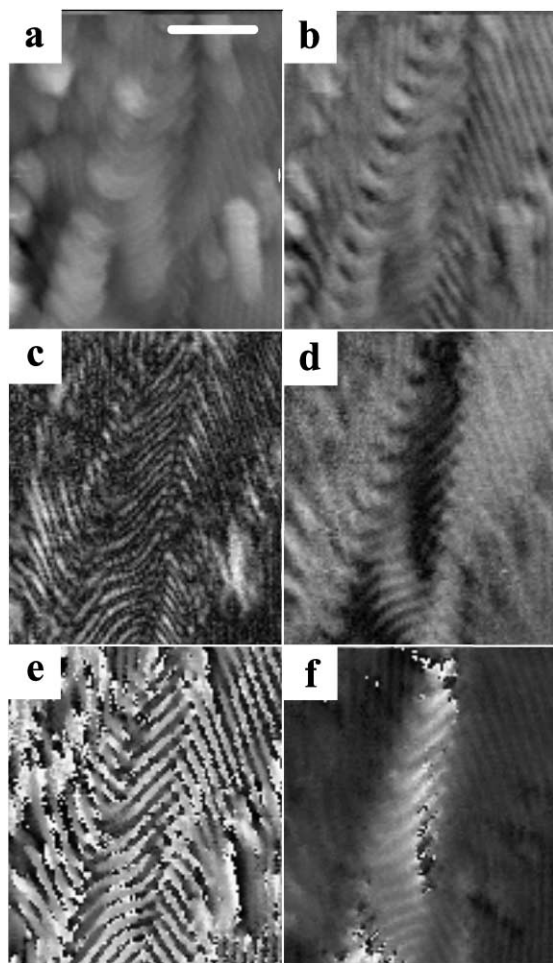
FIG. 3. PM-NSOM images of PS-*b*-PI symmetric tilt boundary. (a) Topography [0 nm, 25 nm]; (b) transmission [0.8, 1.0]; (c) diattenuation [0%, 9%]; (d) retardance [$0°$, $7°$]; (e) relative angle of diattenuating axis [$0°$, $180°$]; (f) relative angle of fast axis [$0°$, $180°$]. White scale bar in (a) is 1 μm.

NSOM studies of polymer systems [23] have observed qualitative chain alignment effects, the PM-NSOM images shown in Figs. 3(d) and 3(f) directly gauge both the degree and angle of molecular orientation, thereby providing insight into both the mesoscale structure and optical activity of these specimens.

In conclusion, we examined ultrahigh-M_r BC specimens with visible light using an improved PM-NSOM technique that explicitly corrects for tip properties. Micrographs that map optical transmission, birefringence, and diattenuation with resolution sufficient to probe the structure of individual microdomains and defects in BC systems are shown. Such characterization will become increasingly important as BC-based photonic systems become more sophisticated, and include, for example, liquid crystalline components and chromophores.

*Present address: Polymers Division, NIST, Gaithersburg, MD 20899-8542.

†Corresponding author.

[1] J. D. Joannopoulos, R. D. Meade, and J. N. Winn, *Photonic Crystals* (Princeton University Press, Princeton, NJ, 1995); P. A. Rundquist *et al.*, J. Chem. Phys. **91**, 4932 (1989); A. Imhof and D. J. Pine, Nature (London) **389**, 948 (1997).

[2] Y. Fink *et al.*, J. Lightwave Technol. **17**, 1963 (1999).

[3] A. Urbas, Y. Fink, and E. L. Thomas, Macromolecules **32**, 4748 (1999); A. Urbas *et al.*, Adv. Mater. **12**, 812 (2000); A. C. Edrington *et al.*, Adv. Mater. **13**, 421 (2001).

[4] M. Maldovan *et al.*, Phys. Rev. B **65**, 165123 (2002); A. M. Urbas and E. L. Thomas, Adv. Mater. **14**, 1850 (2002).

[5] F. S. Bates and G. H. Fredrickson, Annu. Rev. Phys. Chem. **41**, 525 (1990); E. L. Thomas and R. L. Lescanec, Philos. Trans. R. Soc. London **348**, 149 (1994).

[6] See M. J. Fasolka and A. M. Mayes, Annu. Rev. Mater. Res. **31**, 323 (2001).

[7] E. H. Synge, Philos. Mag. **6**, 356 (1928); D. W. Pohl, W. Denk, and M. Lanz, Appl. Phys. Lett. **44**, 651 (1984).

[8] E. Betzig *et al.*, Science **251**, 1468 (1991).

[9] E. Betzig, P. L. Finn, and J. S. Weiner, Appl. Phys. Lett. **60**, 2484 (1992).

[10] S. J. Johnson, P. L. Frattini, and G. G. Fuller, J. Colloid Interface Sci. **104**, 440 (1985); D. A. Higgins *et al.*, J. Phys. Chem. **100**, 13 794 (1996).

[11] E. B. McDaniel, S. C. McClain, and J. W. P. Hsu, Appl. Opt. **37**, 84 (1998).

[12] J. W. P. Hsu, Mater. Sci. Eng. **33**, 1 (2001).

[13] P. DeRose, J. Hwang, and L. S. Goldner, in *Laser Techniques for Surface Science*, SPIE Proceedings Vol. 3272 (SPIE—International Society for Optical Engineering, Bellingham, WA, 1998), p. 93.

[14] L. S. Goldner *et al.*, Appl. Opt. (to be published).

[15] P. N. Minh *et al.*, J. Microsc. **202**, 28 (2001).

[16] P. K. Wei and W. S. Fann, J. Microsc. **202**, 148 (2001).

[17] A. L. Campillo and J. W. P. Hsu, J. Appl. Phys. **91**, 646 (2002).

[18] R. J. Albalak and E. L. Thomas, J. Polym. Sci. **32**, 341 (1994).

[19] A. L. Campillo, J. W. P. Hsu, and G. W. Bryant, Opt. Lett. **27**, 415 (2002).

[20] H. A. Bethe, Phys. Rev. **66**, 163 (1944); C. J. Bowkamp, Philips Res. Rep. **5**, 321 (1950); **5**, 401 (1950).

[21] *Polymer Handbook*, edited by J. Brandrup, E. H. Immergut, and E. A. Grulke (John Wiley & Sons, Inc., New York, 1999), 4th ed.

[22] M. Hashiyama, R. G. Gaylord, and R. S. Stein, Makromol. Chem. Suppl. **1**, 579 (1975).

[23] C. H. Tan *et al.*, J. Phys. Chem. Solids **62**, 1643 (2001); J. Teetsov and D. A. Vanden Bout, J. Phys. Chem. B **104**, 9378 (2000); R. L. Williamson and M. J. Miles, J. Vac. Sci. Technol. B **14**, 809 (1996); H. Ade *et al.*, Langmuir **12**, 231 (1996); D. A. Higgins *et al.*, J. Phys. Chem. B **105**, 5874 (2001).